Paesano: Holonomic Autonomous Mobile Robotics Platform

Architecture, Estimation, and Control

Joseph Marra

April 23, 2026

Abstract

Paesano is a holonomic indoor mobile robotics platform designed around a Raspberry Pi 5 for high-level autonomy processes and a Raspberry Pi Pico-based low-level motor-control module. The project was motivated by a specific robotics problem: achieving consistent and reliable indoor navigation in ambiguous and complex environments without relying on external positioning infrastructure. The final system integrates wheel odometry, IMU fusion through an Extended Kalman Filter, Monte Carlo Localization with a likelihood-field model using LiDAR data, a custom inflated clearance-aware cost map, planning with A* on this cost map, spline-based trajectory generation, and Linear Quadratic Regulator path tracking. A custom iOS mobile application provides teleoperation, mode management, live map and localization visualization, and navigation control. This is done through an HTTP and WebSocket bridge running on the robot. Two experiments were conducted to evaluate Paesano. The first measured low-level velocity and stop behavior across forward, lateral, and rotational commands. The second evaluated full-stack trajectory-following performance. Across nine navigation trials, the system achieved a mean cross-track error of 0.0088 m and a mean final position error of 0.0059 m in the LiDAR-localized map frame, along with a 100% route-completion success rate. These results indicate consistent and repeatable map-frame navigation performance. The complete listed bill of materials totals approximately $644.04.

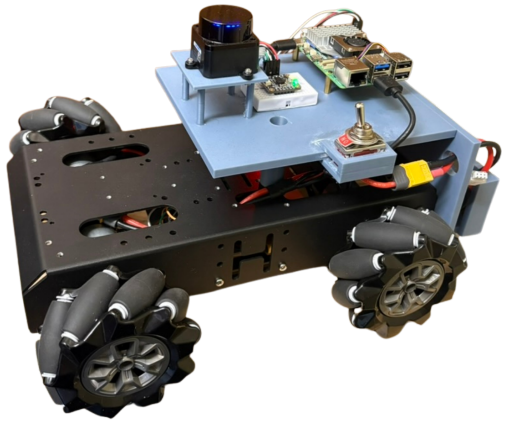

Figure 1: Paesano.

Contents

1 Hardware Architecture **4**

1.1 Parts List 4

1.1.1 Additional Required Tools 4

1.2 System Overview 4

1.3 Power Architecture 5

1.4 Motor Control Stack 6

1.5 Sensor Suite 6

1.6 Mechanical Design 7

1.7 Design Philosophy 7

2 Firmware **8**

2.1 Communication Protocol 8

2.2 Control Loop Architecture 8

2.3 Motor Control Algorithms 9

2.3.1 Velocity PID Control 9

2.3.2 Position PID Control 9

3 Software Architecture **10**

4 Kinematics **11**

5 Odometry **12**

6 State Estimation **13**

6.1 Extended Kalman Filter (EKF) 13

6.1.1 Purpose in the System 13

6.1.2 State Vector 13

6.1.3 Covariance Tuning 14

6.2 Monte Carlo Localization (MCL) 14

6.2.1 Purpose in the System 14

6.2.2 Bayesian Formulation 15

6.2.3 Motion Model . . . 15
6.2.4 Measurement Model (Likelihood Field Model) . . . 16
6.2.5 Resampling . . . 18
6.3 Kidnapped Robot Problem . . . 18
6.3.1 Limitations and Failure Modes . . . 20

7 Navigation **20**
7.1 Occupancy Grid Model . . . 20
7.2 A^* . . . 21
7.3 Geometric Path Post-Processing and Trajectory Synthesis . . . 21
7.3.1 Path Pruning: String Pull . . . 21
7.3.2 Path Smoothing and Arc-Length Parameterization . . . 22

8 Trajectory Following **22**
8.1 Linear Quadratic Regulator (LQR) . . . 22

9 Mobile Application **24**

10 Experiments **25**
10.1 Velocity and Position Control Performance . . . 25
10.2 Trajectory Following Performance . . . 27

11 Conclusion and Future Improvements **30**
11.1 Conclusion . . . 30
11.2 Problems Encountered . . . 30
11.3 Future Improvements . . . 31

1 Hardware Architecture

1.1 Parts List

Prices shown below are approximate and may fluctuate over time based on vendor availability, shipping, and market conditions. Total estimated cost of listed components: $644.04.

Table 1: Bill of materials for the Paesano platform.

Part	Cost (USD)
HiWonder Chassis Kit	$185.00 (approx.)
PCB Kit (prototype PCB, headers, and assembly materials)	$9.99
Raspberry Pi 5 w/ Power Supply and Active Cooler	$162.99
LD19 LiDAR	$74.90
Buck Converter (USB-C 5V 5A)	$9.99
22AWG Arduino Wires (Assorted)	$6.98
Power Switch	$7.99
Standoffs	$7.99
Heat Shrink	$7.99
5V Buck Converter	$8.99
5200mAh LiPo Battery	$35.99
LiPo Charger	$39.98
Raspberry Pi Pico (3x)	$14.59
XT60 Connectors	$10.99
XT60 1-to-2 Splitter	$12.88
BNO085	$24.95
Motor Drivers	$9.90
Wago Connectors	$11.95

1.1.1 Additional Required Tools

- Assorted screwdrivers
- Soldering iron
- Multimeter
- Access to a 3D printer

1.2 System Overview

Paesano is built so that it separates high-level processing from low-level and noisy motor control. The high-level compute module (Raspberry Pi 5 (RPI5) running Ubuntu LTS 24.04) handles state estimation, navigation, and high-level control/planning, while the motor control module (Raspberry Pi Pico (Pico), and TB6612 Motor Drivers) manages low-level actuation of motors. This separation allows future upgrades or repairs to parts without significant redesign of the entire system. The

RPI5 receives and processes sensor data and uses it for state estimation and navigation, then sends control commands to the motor control module, which then actuates the motors accordingly.

Figure 2 shows the resulting system architecture and the primary flow of power and information between components.

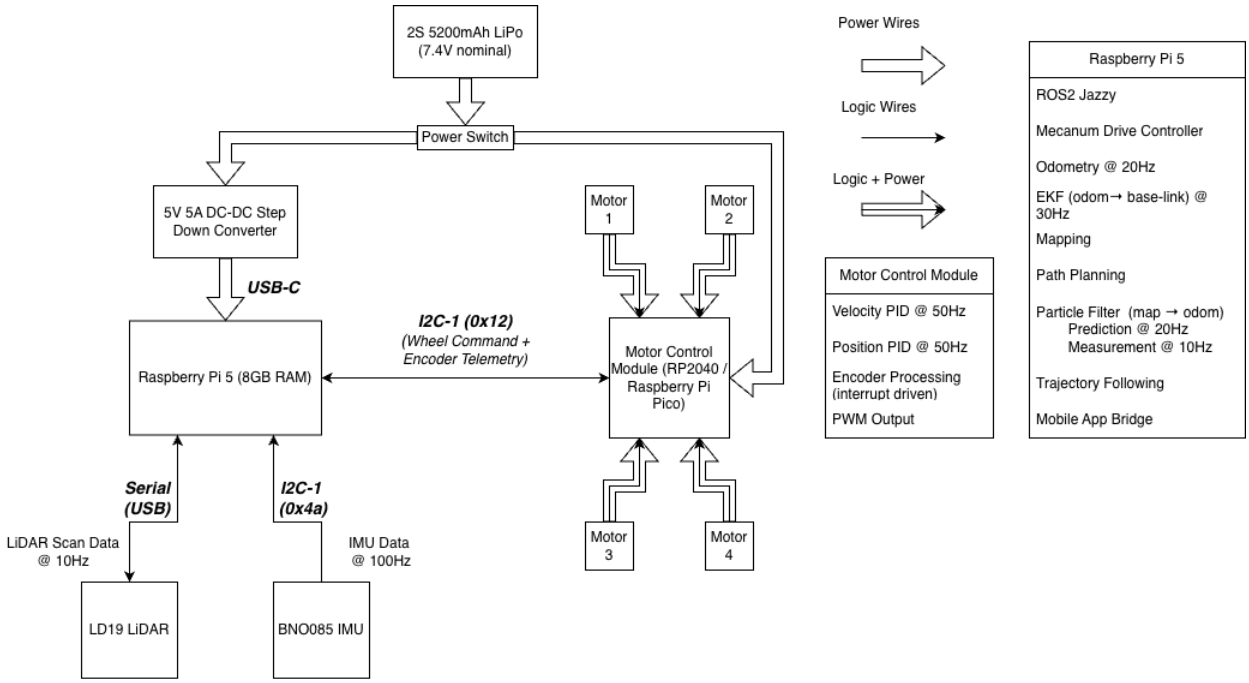

Figure 2: System architecture overview.

1.3 Power Architecture

The robot is powered by a 7.4 V nominal 2S 5200 mAh LiPo battery which was selected for its high energy density and ability to provide the necessary current for all components, especially the motor drivers. For stable power delivery, a dedicated DC-DC converter is used to regulate the battery supply to the voltage/current levels required by the RPI5. The motors themselves are powered directly from the 7.4 V supply, since they are designed to operate at this voltage. The Pico is powered from a regulated 5 V rail within the motor control module.

1.4 Motor Control Stack

The HiWonder chassis originally came with its own motor control module and PID controller. However, the available hardware was limited and the firmware was not practical to customize for this project. A dedicated motor control module was therefore designed around the Pico and two TB6612 dual motor drivers.

This motor control module performs closed-loop control of the four DC motors at a fixed update rate of 50 Hz. Offloading these tasks to a microcontroller keeps the low-level loop deterministic and allows the Raspberry Pi 5 to reserve its compute resources for higher-level autonomy tasks. Figure 3 shows the schematic of this subsystem.

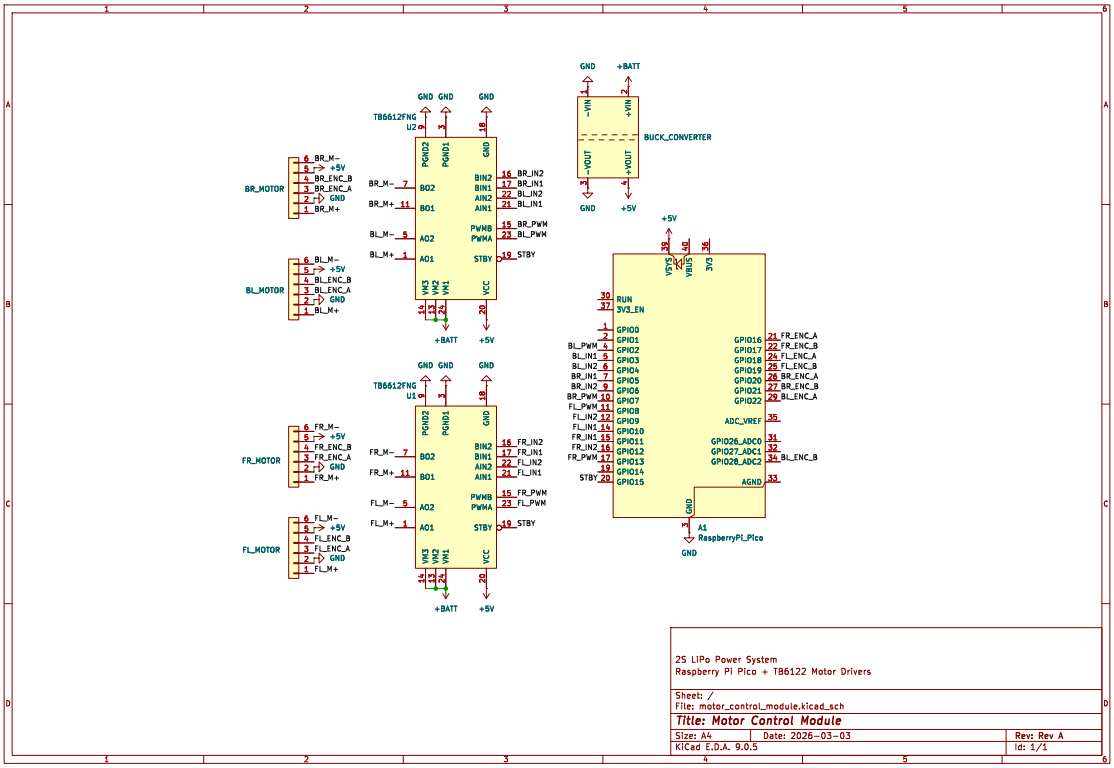

Figure 3: Motor Control Module.

1.5 Sensor Suite

The robot uses a combination of wheel encoders, IMU, and LiDAR for perception and state estimation. A BNO085 IMU provides orientation and angular velocity measurements at approximately 100 Hz. IMU data is fused with wheel odometry (20 Hz, calculated using wheel encoders) in an Extended Kalman Filter to produce a smooth local state estimate. An LD19 2D LiDAR sensor provides planar range measurements which are used for mapping and localization. The scan data is produced at approximately 10 Hz.

- IMU Datasheet/Documentation: `https://www.adafruit.com/product/4754`
- LiDAR Datasheet/Documentation: `https://wiki.youyeetoo.com/en/Lidar/D300`

1.6 Mechanical Design

The chassis from HiWonder provided motors with encoders and a main chassis frame. However, it did not come with any intuitive way to mount the various sensors, batteries, and other processing units. To address this, several custom parts were designed to integrate these systems into the platform. These parts were designed using OnShape and then printed on a Bambu Lab X1 Carbon in PLA.

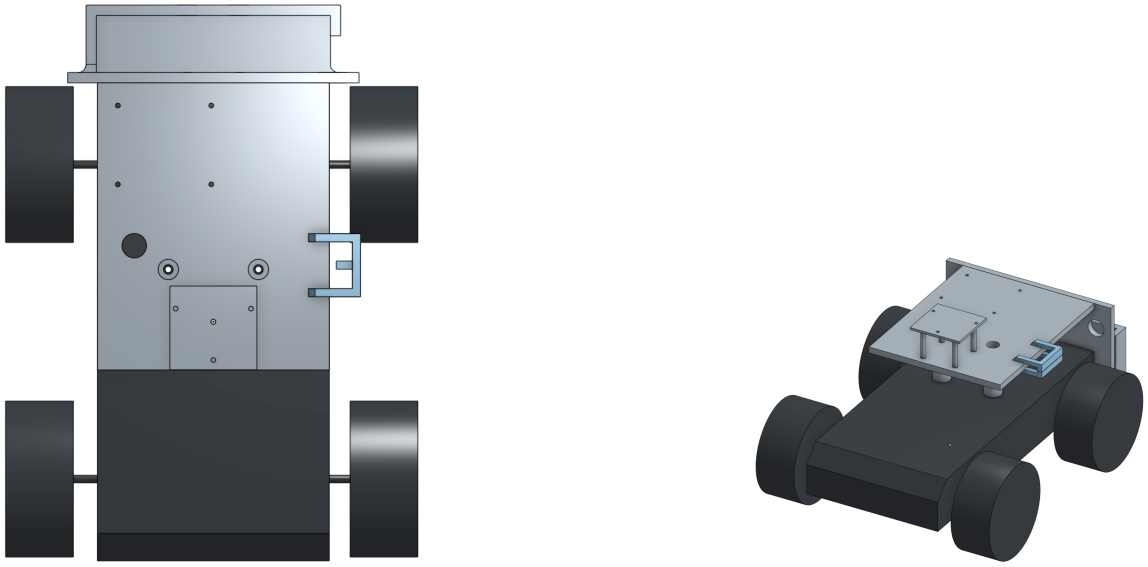

(a) CAD Bird's Eye View

(b) CAD Isometric View

Figure 4: Mechanical CAD models of the platform and custom mounts.

The parts in gray and in blue are the ones that were custom designed and printed. The part in black is a model of the HiWonder chassis to make designing the custom parts easier. The parts in gray include a stand for the LiDAR, a mounting plate for the Raspberry Pi 5 and IMU, and a battery compartment in the back. The blue part is a power switch holder, and once printed it is to be super glued onto the gray mounting plate wherever desired.

1.7 Design Philosophy

The platform was designed around modularity, simplicity, expandability, accessibility, and cost effectiveness.

- Modularity: low-level motor control is isolated from the autonomy stack, and the major ROS 2 subsystems communicate through explicit and standardized interfaces. This made it practical to debug and revise one layer without destabilizing the rest of the robot.

- Simplicity: The design prioritizes straightforward implementation and maintenance, ensuring that the robot can be easily understood and modified by developers.
- Expandability: The platform is designed to accommodate future enhancements and modifications, with spare compute headroom, open mounting space, and software abstraction layers preserved for future sensors or estimation methods.
- Accessibility: The design ensures that components are easily accessible for maintenance and upgrades, without requiring too much disassembly.
- Cost Effectiveness: Component selection was influenced by the need to balance performance with cost, ensuring that the platform remains practical and affordable while meeting its functional requirements.

2 Firmware

All firmware for this project was written in C++ for compatibility with the RP2040 microcontroller on the Pico and for superior performance. The firmware is responsible for real-time motor control, encoder processing, and communication with the RPI5.

2.1 Communication Protocol

Communication between the Raspberry Pi 5 and the Pico is implemented over I^2C, with the Raspberry Pi 5 acting as the bus master and the Pico configured as an I^2C slave at address `0x12`. The Raspberry Pi 5 reads and writes register-mapped data to exchange control commands and telemetry.

Table 2: I^2C register map between the Raspberry Pi 5 and Pico.

Name	Address/Register	Pico Access	Purpose
`I2C_ADDR`	`0x12`	N/A	7-bit I^2C slave address for the Pico.
`REG_MOTOR_SPEEDS`	`51`	Read	Sets wheel/motor speed targets.
`REG_ENCODERS`	`60`	Write	Readback register for encoder counts.
`REG_PID_GAINS`	`70`	Read	Configuration register for PID gain parameters.

In Table 2, the *Pico Access* column is written from the Pico's perspective as the I^2C slave. A register marked *Read* is read by the Pico when the Raspberry Pi writes into it, while a register marked *Write* is written by the Pico so the Raspberry Pi can read the resulting telemetry.

2.2 Control Loop Architecture

The main control loop of the firmware runs every 0.02 s, or at 50 Hz. Encoder measurements are used to estimate wheel velocities, which are fed into a cascaded control system. There are two possible modes: drive and hold.

In drive mode, the robot moves at the commanded velocity using a velocity PID with feedforward compensation. In hold mode (after the robot has been commanded to stop), a position controller generates velocity targets based on the error between the current position and the position at the time the robot was commanded to stop so it remains in place. These targets are then tracked by the velocity PID controller. The resulting PWM signals from either mode are sent to the TB6612 motor drivers.

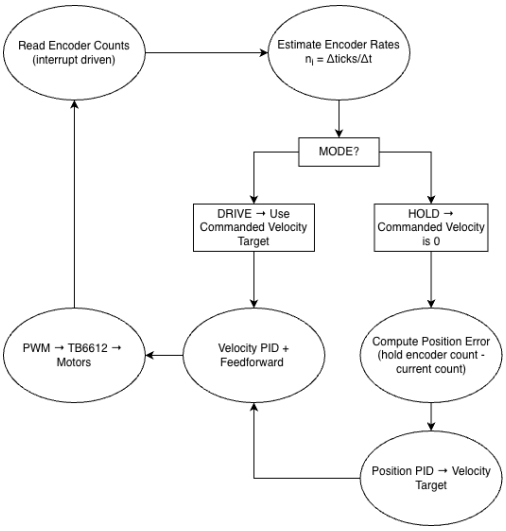

Figure 5: Control loop timing diagram.

2.3 Motor Control Algorithms

As described above, motor velocity and position control is done using separate velocity and position PID controllers. The expressions below describe the control laws conceptually using time-domain notation for readability, even though the firmware runs them discretely at 50 Hz. To overcome static friction and actively track the target before any feedback compensation, a linear plus static-friction feedforward term is added to the velocity control algorithm. Also, the I term in both controllers is conditionally updated to prevent windup when the output saturates.

2.3.1 Velocity PID Control

$$e_v(t) = v_{\text{ref}}(t) - v(t)$$

$$u_v(t) = K_{p,v} e_v(t) + K_{i,v} I_v(t) - K_{d,v} \frac{dv(t)}{dt} + K_{\text{ff}}\, v_{\text{ref}}(t) + K_s\, \text{sgn}(v_{\text{ref}}(t))$$

where the static term is only applied for nonzero commanded wheel speed.

2.3.2 Position PID Control

$$e_p(t) = p_{\text{ref}}(t) - p(t)$$

$$v_{\text{ref}}(t) = K_{p,p}e_p(t) + K_{i,p}I_p(t) + K_{d,p}\frac{de_p(t)}{dt}$$

In the implementation (and as seen in the control loop timing diagram), the velocity controller handles normal motion tracking while the position controller is only engaged after a stop command. This arrangement keeps the robot responsive during motion and reduces residual drift once the commanded velocity returns to zero.

3 Software Architecture

The software (in C++) in the high-level compute module, running on the Raspberry Pi 5 (RPI5), is built using the Jazzy Jalisco distribution of ROS 2 on Ubuntu 24.04 LTS. ROS2 provides a modular architecture that allows complex robotic systems such as this to be composed of smaller independent nodes, communicating over standardized topics. Using ROS2 provides several advantages for this system. First, it enables clear separation between the subsystems of perception, state estimation, planning, and control, where each system is its own node or series of nodes. Second, the publish-subscribe communication model used by ROS2 topics makes it simple to route sensor data and commands between nodes.

In this system, sensor measurements such as wheel encoder data, IMU readings, and LiDAR scans are published on dedicated topics and used by estimation nodes that fuse these measurements to produce a consistent state estimate of the robot. Higher level nodes for navigation and trajectory following use this state estimation. Robot commands are eventually published as velocity commands which are sent to the motor control module to convert them into actual motor actuation commands.

The mobile bridge runs as both a ROS 2 node and a FastAPI/Uvicorn server, and switches modes by restarting bringup with the localization mode launch argument set appropriately.

The TF frame tree defines the relationships between the robot base (`base_link`), odometry frame (`odom`), map frame (`map`), and onboard sensors (`base_laser`, `imu_link`). These transforms are used by localization, navigation, and control nodes so that pose estimates and commands remain consistent across the full software stack.

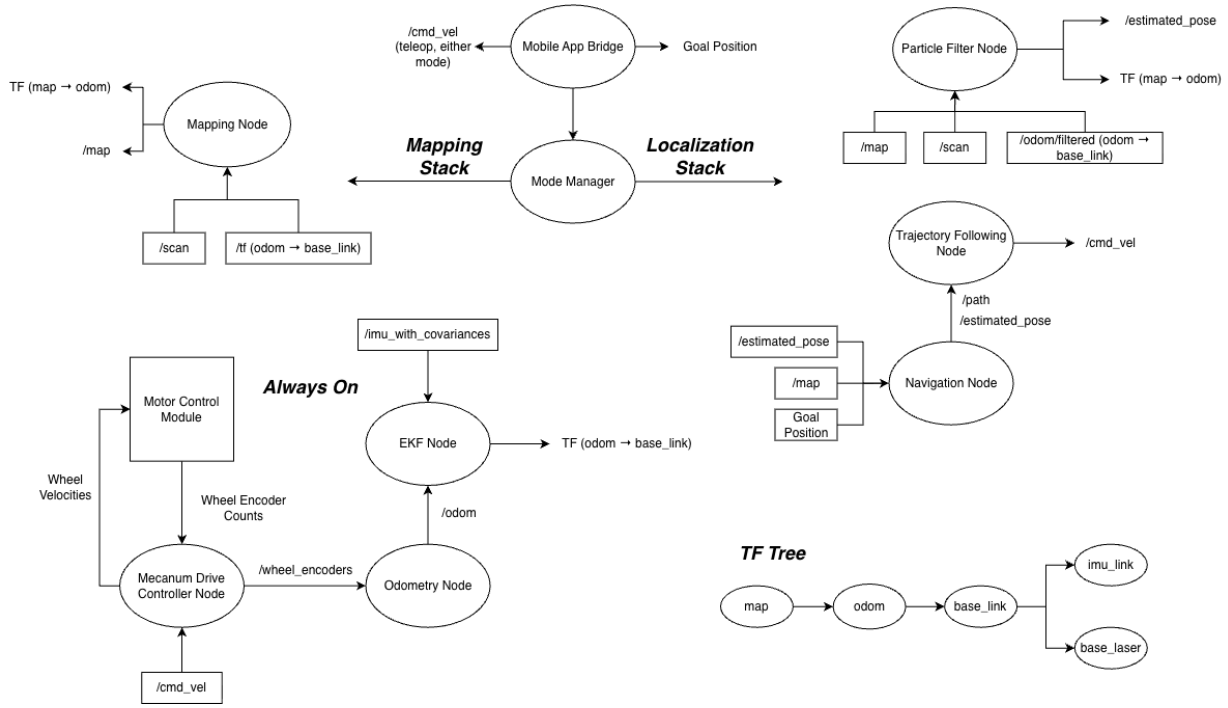

Figure 6: Software architecture overview.

4 Kinematics

To achieve holonomic motion, the robot uses a mecanum wheel drivetrain. While a system such as swerve drive offers superior traction, efficiency, and high-speed performance, it also requires additional steering motors and more complex mechanical control systems. For this project, that increased complexity was not justifiable on a time or budget basis.

Mecanum drive was chosen because it provides omnidirectional movement using only four drive motors. It is mechanically simple but fully holonomic. A differential-drive robot would have been simpler, but for the purposes of this project, the ability to strafe and rotate was deemed important for navigating tight environments. Additionally, implementing a more complex kinematic model is beneficial for control and learning purposes. The RPI5 interprets `/cmd_vel` in SI units and applies geometry-based inverse kinematics using Paesano's dimensions:

$$r = 0.0485\,\text{m}, \qquad L = 0.212\,\text{m}, \qquad W = 0.194\,\text{m}, \qquad R = \frac{L+W}{2} = 0.203\,\text{m}$$

For a commanded body-frame twist

$$\mathbf{u} = \begin{bmatrix} v_x \\ v_y \\ \omega \end{bmatrix},$$

the wheel rim linear velocities are computed as

$$\begin{bmatrix} v_{\text{FL}} \\ v_{\text{FR}} \\ v_{\text{BL}} \\ v_{\text{BR}} \end{bmatrix} = \begin{bmatrix} 1 & -1 & -R \\ 1 & 1 & R \\ 1 & 1 & -R \\ 1 & -1 & R \end{bmatrix} \begin{bmatrix} v_x \\ v_y \\ \omega \end{bmatrix}$$

where v_x and v_y are the commanded translational velocities in m/s and ω is the commanded yaw rate in rad/s.

These wheel rim velocities are then converted into encoder tick-rate targets using the known encoder resolution of $N_{enc} = 2882$ ticks per revolution. Since the linear distance traveled per encoder tick is

$$d_{\text{tick}} = \frac{2\pi r}{N_{enc}},$$

the target wheel tick rates become

$$\dot{n}_i = \frac{v_i}{d_{\text{tick}}} = v_i \frac{N_{enc}}{2\pi r}.$$

To keep the commanded motion within the measured hardware envelope, the body-frame command is first clamped to

$$\sqrt{v_x^2 + v_y^2} \leq 0.35\,\text{m/s}, \qquad |\omega| \leq 1.5\,\text{rad/s}.$$

After inverse kinematics, if any wheel target exceeds the configured maximum of 3500 ticks/s, all four wheel targets are scaled by the same factor so that the requested motion direction is preserved while remaining inside the actuator limits. The final tick-rate targets are then normalized to the Pico's signed `int8` command range before being sent over I^2C.

5 Odometry

Wheel odometry provides a local estimate of robot motion by integrating measured wheel velocities over time. This estimate is subject to drift due to wheel slip, friction, noise, and other factors, but it provides a high-frequency state estimate that becomes useful for localization later on. It is calculated using encoder measurements from each of the four drive motors. Each one provides incremental encoder counts (approximately 2882 per revolution) which are first converted to encoder tick rates and then to wheel linear speeds. From these measurements the robot body velocity is estimated and then integrated to produce a pose estimate in the odom frame.

Let Δn_i denote the change in encoder ticks for wheel i over a time interval Δt. The implementation first computes the encoder tick rate

$$\dot{n}_i = \frac{\Delta n_i}{\Delta t}$$

and then converts it into wheel rim linear speed using the measured distance per encoder tick

$$d_{\text{tick}} = \frac{2\pi r}{2882}, \qquad v_i = \dot{n}_i d_{\text{tick}}.$$

The robot velocity is then estimated using the mecanum wheel forward kinematics. Using the same geometry parameter $R = \frac{L+W}{2}$ introduced above, this matrix maps the individual wheel velocities to the robot translational velocity and angular velocity:

$$\begin{bmatrix} v_{x,\text{body}} \\ v_{y,\text{body}} \\ \omega \end{bmatrix} = \begin{bmatrix} \frac{1}{4} & \frac{1}{4} & \frac{1}{4} & \frac{1}{4} \\ -\frac{1}{4} & \frac{1}{4} & \frac{1}{4} & -\frac{1}{4} \\ -\frac{1}{4R} & \frac{1}{4R} & -\frac{1}{4R} & \frac{1}{4R} \end{bmatrix} \begin{bmatrix} v_{\text{FL}} \\ v_{\text{FR}} \\ v_{\text{BL}} \\ v_{\text{BR}} \end{bmatrix}$$

This body-frame velocity is then rotated into the odom frame using the current heading θ:

$$\begin{bmatrix} v_{x,\text{odom}} \\ v_{y,\text{odom}} \end{bmatrix} = \begin{bmatrix} \cos\theta & -\sin\theta \\ \sin\theta & \cos\theta \end{bmatrix} \begin{bmatrix} v_{x,\text{body}} \\ v_{y,\text{body}} \end{bmatrix}$$

The robot pose is then updated by integrating this velocity in the odom frame:

$$\begin{aligned} x_{t+1} &= x_t + v_{x,\text{odom}}\Delta t \\ y_{t+1} &= y_t + v_{y,\text{odom}}\Delta t \\ \theta_{t+1} &= \theta_t + \omega\Delta t \end{aligned}$$

The resulting `/odom` message therefore carries pose in the `odom` frame and twist in the `base_link` frame. The odometry node does not publish TF directly; the `odom` → `base_link` transform is later produced by the EKF.

6 State Estimation

State estimation is split into local (Extended Kalman Filter) and global (Monte Carlo Localization) layers. The EKF fuses wheel odometry and IMU data to produce a smooth local estimate in the odom frame. However, it is still subject to slip and drift. In the current launch structure, the EKF runs in both mapping and localization modes. Monte Carlo Localization (MCL) is only launched in localization mode, where it uses LiDAR and the known map to correct that drift. The EKF publishes `/odom/filtered` together with `odom` → `base_link`, while MCL publishes `/estimated_pose` and `map` → `odom`, giving:

$$^{map}T_{base\_link} = {}^{map}T_{odom}\,{}^{odom}T_{base\_link}$$

6.1 Extended Kalman Filter (EKF)

For this project, the EKF provided by the *robot_localization* package was used for simplicity of integration (`https://wiki.ros.org/robot_localization`).

6.1.1 Purpose in the System

The purpose of the EKF is to generate a high-frequency local state estimate of linear and angular position and velocity by fusing sensor data from wheel odometry and the IMU, using covariance matrices to represent the relative uncertainty of each sensor. A concurrently running node takes the raw IMU, assigns covariance values to the message, and republishes it to a new topic. This IMU stream is then fused with `/odom` using the EKF. This local estimate is used as the motion model input for MCL. An EKF was chosen because it provides a reasonable balance between estimation accuracy and computational efficiency while handling nonlinearity in the motion model.

6.1.2 State Vector

The EKF estimates a six-dimensional state representing the robot's planar pose and velocity.

$$\mathbf{x} = [x, y, v_x, v_y, \theta, \dot{\theta}]^T$$

Odometry x, y, v_x, v_y, θ, $\dot{\theta}$ and IMU θ, $\dot{\theta}$ were fused to estimate this state. However, since odometry θ and $\dot{\theta}$ are extremely unreliable, the covariance matrices were tuned so that odometry primarily informs x, y, v_x, and v_y, while the IMU primarily informs θ and $\dot{\theta}$.

6.1.3 Covariance Tuning

The covariance values used for the EKF were informed by experimental odometry measurements. While the experiment was conducted in ideal conditions, the results reveal important relative characteristics of the drivetrain noise. The experiment shows that forward motion produces the lowest odometry error, while lateral (strafing) motion exhibits significantly higher uncertainty due to the inherent slip characteristics of mecanum wheels. Rotational motion introduces the largest error. Across the trials, this is the relationship between each covariance:

$$\sigma_y^2 \approx 10\sigma_x^2, \qquad \sigma_\theta^2 \approx 10\sigma_y^2$$

Figure 7: EKF covariance tuning reference.

Because the experiments were conducted under ideal conditions, the resulting covariance values represent optimistic estimates of drivetrain noise. In practice, only two covariance design values had to be tuned: a base covariance and a position-versus-velocity scale factor. The base covariance was assigned to forward motion, while lateral and rotational covariances were set to 10x and 100x that value respectively, following the experimental results. The position-versus-velocity scale factor was set to 0.5, since position is the integral of velocity and velocity generally experiences less noise amplification. IMU covariance was initially estimated from the datasheet noise standard deviation, converted to variance, and then tuned experimentally.

6.2 Monte Carlo Localization (MCL)

6.2.1 Purpose in the System

Monte Carlo Localization was chosen because it is able to handle non-Gaussian uncertainty, multi-modal pose hypotheses, and odometry drift. In this system it acts as the global localization layer

on top of the EKF, using LiDAR and the known map to correct accumulated drift in the odom frame. It also pairs naturally with the likelihood-field measurement model and can recover from poor initial pose estimates through reweighting and resampling.

6.2.2 Bayesian Formulation

Monte Carlo Localization is derived from the recursive Bayes filter. The belief over the robot state is updated using both the motion model and the sensor model:

$$bel(w_t) = \eta\, p(z_t \mid w_t) \int p(w_t \mid w_{t-1}, u_t)\, bel(w_{t-1})\, dw_{t-1} \tag{1}$$

where

$$w_t = \begin{bmatrix} x_t \\ y_t \\ \theta_t \end{bmatrix}$$

represents the robot pose at time t.

6.2.3 Motion Model

The motion model uses odometry increments to propagate each particle. First, the odometry displacement is rotated into the robot body frame:

$$\begin{bmatrix} \Delta x_{body} \\ \Delta y_{body} \end{bmatrix} = \begin{bmatrix} \cos(\theta_{odom,t-1}) & \sin(\theta_{odom,t-1}) \\ -\sin(\theta_{odom,t-1}) & \cos(\theta_{odom,t-1}) \end{bmatrix} \begin{bmatrix} \Delta x_{odom} \\ \Delta y_{odom} \end{bmatrix}$$

where $\theta_{odom,t-1}$ is the odometry heading at time $t-1$. The body-frame displacement is then rotated into the frame of the particle:

$$\begin{bmatrix} \Delta x_{part} \\ \Delta y_{part} \end{bmatrix} = \begin{bmatrix} \cos(\theta_{part,t-1}) & -\sin(\theta_{part,t-1}) \\ \sin(\theta_{part,t-1}) & \cos(\theta_{part,t-1}) \end{bmatrix} \begin{bmatrix} \Delta x_{body} \\ \Delta y_{body} \end{bmatrix}$$

The particle state is then updated as

$$\begin{aligned} x_t &= x_{t-1} + \Delta x_{part} \\ y_t &= y_{t-1} + \Delta y_{part} \\ \theta_t &= \theta_{t-1} + \Delta \theta_{odom} \end{aligned}$$

To model uncertainty in the propagated particle state, the motion model is represented as a 3D Gaussian with covariance

$$\Sigma_t = \begin{bmatrix} (x_{\text{noise}} \cdot translation)^2 & 0 & 0 \\ 0 & (y_{\text{noise}} \cdot translation)^2 & 0 \\ 0 & 0 & (\theta_{\text{noise}} \cdot rotation)^2 \end{bmatrix}.$$

After applying the odometry increment to each particle, Gaussian noise is added to model uncertainty in the motion estimate for each particle:

$$\hat{w}_t = \begin{bmatrix} \bar{x}_t \\ \bar{y}_t \\ \bar{\theta}_t \end{bmatrix} + \epsilon_t, \qquad \epsilon_t \sim \mathcal{N}(0, \Sigma_t).$$

6.2.4 Measurement Model (Likelihood Field Model)

A likelihood field model scores each particle by projecting the observed LiDAR beams from that particle pose and computing the expected beam endpoints in the map. It then queries the distance from each endpoint to the nearest known obstacle in the precomputed distance field. The per-beam likelihood is represented as a Gaussian-uniform mixture:

- Z_{hit}: probability that a reading was generated by a correct geometrical interaction with the map.
- Z_{rand}: probability that a reading was generated by random noise or unmodeled geometry.
- The mixture weights satisfy $Z_{hit} + Z_{rand} = 1$.

In this model, the Gaussian hit term is

$$P_{hit} = Z_{hit} \cdot \mathcal{N}(d_i; 0, \sigma^2)$$

and the uniform random term is

$$P_{rand} = Z_{rand} \cdot \frac{1}{Z_{max}},$$

where d_i is the beam-endpoint distance to the nearest obstacle and Z_{max} is the maximum LiDAR range.

The mixture model prevents any single incorrect reading from collapsing the particle likelihood to zero. For example, if a reading is 5 m from the nearest obstacle, its Gaussian term in log space becomes

$$\ln\left(\exp\left(\frac{-d^2}{2\sigma^2}\right)\right) = \ln(\exp(-1250))$$

In exact mathematics this is simply -1250, but in floating-point arithmetic $\exp(-1250)$ underflows to zero and would force the code to evaluate $\ln(0)$. The uniform term prevents that failure mode by assigning a small nonzero likelihood to unexpected readings:

$$P(z_i|x) = P_{hit} + P_{rand}$$

Here z_i denotes a single beam and x denotes the particle pose. For a full scan containing k beams, the total likelihood is

$$P(Z|x) = \prod_{i=1}^{k} P(z_i|x)$$

Because each $P(z_i|x)$ is less than 1, this product underflows quickly, so the implementation accumulates scan likelihood in log space:

$$\ln(P(Z|x)) = \sum_{i=1}^{k} \ln(P(z_i|x))$$

For each beam, however, the measurement model is itself a mixture:

$$P(z_i \mid x) = P_{hit} + P_{rand}.$$

This means the per-beam log likelihood cannot be written as the sum of the individual log terms. Instead, the implementation evaluates

$$\ln(P_{hit} + P_{rand})$$

The logarithms of the two mixture components are computed separately and combined using the log-sum-exp identity. The full scan product is accumulated in log space to avoid underflow across many small beam probabilities. Log-sum-exp is then used inside each beam because the hit and random mixture terms still have to be added while remaining in log space:

$$a = \ln(P_{hit})$$

$$b = \ln(P_{rand})$$

$$\ln(P_{hit} + P_{rand}) = \ln(e^a + e^b) = m + \ln(e^{a-m} + e^{b-m})$$

where

$$m = \max(a, b)$$

For each particle, the total scan log likelihood is computed as

$$\log P(Z \mid x) = \sum_{i=1}^{k} \left[m_i + \ln\left(e^{a_i - m_i} + e^{b_i - m_i} \right) \right],$$

where $m_i = \max(a_i, b_i)$. This produces an unnormalized scan log likelihood for each particle. In the implementation, that likelihood is applied multiplicatively to the particle's existing weight and then the result is normalized.

Let

$$c = \max_i \log w_i$$

where $\log w_i$ is the scan log likelihood of particle i. Then define the shifted updated weights

$$\tilde{w}_i = w_{i,t-1} \exp(\log w_i - c).$$

Subtracting the maximum log weight ensures that the largest exponent is zero, which prevents numerical overflow. The normalized particle weights are then

$$w_i = \frac{\tilde{w}_i}{\sum_j \tilde{w}_j},$$

so that

$$\sum_i w_i = 1.$$

6.2.5 Resampling

Resampling is necessary to reduce particle degeneracy, where most particles receive near-zero weight. This process:

- removes low-weight particles
- duplicates high-weight particles
- keeps the particle set focused on likely states
- improves estimation quality for the same compute budget

Resampling is triggered by the effective sample size, which measures how many particles are contributing meaningful weight to the estimate:

$$N_eff = \frac{1}{\sum_{i=1}^{N} w_i^2}$$

Here N is the total number of particles and w_i is the weight of particle i. An effective sample size close to N means most particles contribute meaningfully to the estimate, while a value close to 1 means the estimate is dominated by only a few particles. In the implementation, resampling is triggered when $N_eff < 0.5N$.

Systematic resampling is then performed using the cumulative distribution of normalized particle weights. A single random offset $r \sim \mathcal{U}(0, 1/N)$ is chosen, and evenly spaced sample locations $u_i = r + (i-1)/N$ are swept through the cumulative distribution. The random offset is chosen so that we don't always sweep over the same particles, which would reduce diversity. After resampling, all particle weights are reset to $1/N$, and small Gaussian offsets are added to the resampled particles to reduce particle impoverishment.

6.3 Kidnapped Robot Problem

To address the kidnapped robot problem, an adaptive random particle injection strategy was implemented. Given a set of particle log-likelihoods $\ell_i = \log p(z \mid x_i)$, the mean likelihood across particles is computed in a numerically stable manner using log-sum-exp:

$$\log \sum_i e^{\ell_i} = \ell_{\max} + \log \sum_i e^{\ell_i - \ell_{\max}}$$

The average likelihood is then:

$$\log \bar{p} = \log \left(\frac{1}{N} \sum_i e^{\ell_i} \right) = \ell_{\max} + \log \sum_i e^{\ell_i - \ell_{\max}} - \log N$$

To normalize for the number of laser beams B, a scan quality metric is defined as

$$q = \exp\left(\frac{\log \bar{p}}{B}\right)$$

Two exponential moving averages are maintained:

$$w_{\text{fast}} \leftarrow w_{\text{fast}} + \alpha_{\text{fast}}(q - w_{\text{fast}})$$
$$w_{\text{slow}} \leftarrow w_{\text{slow}} + \alpha_{\text{slow}}(q - w_{\text{slow}})$$

The ratio between these averages is used to detect localization degradation:

$$r = \frac{w_{\text{fast}}}{w_{\text{slow}}}$$

Using the ratio of fast and slow averages is superior to reacting to instantaneous confidence alone, since scan quality can fluctuate momentarily due to factors such as unaccounted-for dynamic obstacles or inconsistencies in the known map. The two differently weighted running averages therefore detect a sustained drop relative to the recent baseline, which is a better indicator of the kidnapped robot condition. The difference in weights of these two averages is tuned empirically. An adaptive injection probability is then defined as

$$p_{\text{adapt}} = \text{clamp}(1 - r, 0, 1)$$

This value is used to interpolate between a baseline and maximum random particle percentage:

$$\beta = \text{clamp}(k \cdot p_{\text{adapt}}, 0, 1)$$
$$P_{\text{random}} = P_{\text{base}} + (P_{\text{max}} - P_{\text{base}})\beta$$

The number of injected particles is

$$N_{\text{inject}} = \frac{P_{\text{random}}}{100} \cdot N$$

Injected particles are sampled by choosing random free cells from the map and then perturbing each selected cell uniformly within one map resolution. Let Δ_{map} denote the map resolution:

$$x \sim \mathcal{U}(x_{\text{cell}} - 0.5 * \Delta_{\text{map}},\ x_{\text{cell}} + 0.5 * \Delta_{\text{map}}), \quad y \sim \mathcal{U}(y_{\text{cell}} - 0.5 * \Delta_{\text{map}},\ y_{\text{cell}} + 0.5 * \Delta_{\text{map}}), \quad \theta \sim \mathcal{U}(-\pi, \pi)$$

To improve performance while navigating, adaptive random injection is enabled only when the robot is not navigating, or when its yaw rate remains below the rapid-turn threshold:

$$\text{allow} = (|\dot{\theta}| \leq \tau) \vee (\neg \text{navigating})$$

This prevents spurious particle dispersion caused by scan distortion or intentional motion.

6.3.1 Limitations and Failure Modes

There are a few situations in which the particle filter and adaptive injection strategy may still fail:

- If the robot is navigating and experiences a sudden large disturbance (e.g. colliding with an obstacle), the scan quality may drop significantly while the robot is still moving, which could trigger random particle injection at a time when the filter is already struggling to maintain a coherent pose estimate.
- If the environment contains large ambiguous areas (e.g. long corridors or open spaces) where many poses produce similar scan likelihoods, the particle filter may struggle to converge to a single pose and may require more particles or additional sensor modalities for disambiguation.
- If the map is inaccurate or outdated, the measurement model may produce consistently low likelihoods even when the robot is correctly localized, leading to excessive random particle injection and potential divergence of the filter.

Tuning the particle filter parameters, such as the number of particles, motion noise, and likelihood-field parameters, helped mitigate these failure modes. Under extreme circumstances the filter may still fail, but it is robust enough to handle typical navigation scenarios and to recover from temporary localization degradation.

Together, the EKF and MCL layers provide the state estimate used by the planning and trajectory following stack described in the next section. The EKF maintains a smooth local estimate in the odom frame, while MCL provides the global correction required for map-frame navigation.

7 Navigation

7.1 Occupancy Grid Model

Global planning is performed on a 2D occupancy grid, but the planner does not treat all free cells equally. When A* is run directly on a raw occupancy grid, the resulting path tends to hug walls and produce trajectories that are impractical for the robot to follow. Rather than running A* directly on the raw binary map, the implementation first constructs an **inflated clearance-aware cost map**. This allows the robot to prefer routes that maintain additional distance from obstacles instead of simply finding the shortest geometric path through free space.

The process begins by computing, for every grid cell, the distance to the nearest occupied or unknown cell. Occupied cells and unknown cells are both treated as obstacle sources during this step. A Dijkstra-style expansion over the 8-connected grid is then used to propagate the nearest-obstacle distance throughout the map, producing a clearance field

$$d(\mathbf{c}) = \text{distance from cell } \mathbf{c} \text{ to the nearest obstacle.}$$

A hard safety buffer is then enforced around obstacles. If a cell lies within the configured obstacle buffer distance d_b, it is treated as non-traversable:

$$d(\mathbf{c}) \leq d_b \quad \Longrightarrow \quad \mathbf{c} \text{ is blocked.}$$

For cells outside this buffer, the planner assigns a traversal penalty that decreases as clearance increases. In the implementation, this is a smooth **exponential** cost applied on top of the normal grid step cost:

$$J_{\text{clear}}(\mathbf{c}) = \lambda \exp\left(-\frac{d(\mathbf{c}) - d_b}{\ell}\right), \qquad d(\mathbf{c}) > d_b$$

Here λ is the clearance cost scale and ℓ is the clearance decay length. This means that cells just outside the obstacle buffer still carry a significant cost, while cells farther from obstacles rapidly become inexpensive. As a result, the planner naturally biases paths toward wider, safer corridors without discarding valid narrow passages when they are necessary.

During search, this clearance penalty is added directly to the normal A* step cost for each candidate neighbor. Axis-aligned steps retain a nominal cost of 1, diagonal steps retain a nominal cost of $\sqrt{2}$, and the obstacle-clearance penalty is added to both. The resulting planner is therefore still shortest-path based, but with a traversal model that explicitly favors obstacle clearance rather than minimizing Euclidean length alone.

7.2 A^*

Global path planning is performed using the A* algorithm on the inflated clearance-aware cost map detailed in the previous section. Since the map is discretized into square cells, the raw output of A* is a sequence of adjacent grid coordinates rather than a continuous trajectory. This makes the initial path safe and graph-search optimal with respect to the grid cost model, but it also makes the output inherently jagged. Such a path is not ideal for a physical robot, especially one that will later be tracked by a continuous controller.

In the current implementation, the goal cell must be traversable on the inflated cost map, but the start cell is allowed to lie inside the inflated safety buffer so that the robot can still plan out of a tight location near an obstacle. For this reason, the global planner is treated as the first stage of a path generation pipeline rather than the final trajectory itself. The A* search produces a collision-free sequence of cells, after which geometric post-processing is applied to reduce unnecessary waypoints and convert the discrete path into a smoother trajectory suitable for tracking.

7.3 Geometric Path Post-Processing and Trajectory Synthesis

7.3.1 Path Pruning: String Pull

The first post-processing step is a String Pulling algorithm. Its purpose is to prune redundant intermediate nodes introduced by the grid representation. Rather than forcing the robot to visit every cell transition selected by A*, the string-pull stage searches for the longest obstacle-free straight-line connections between waypoints.

This reduces the path to the minimum number of straight-line segments required to traverse the environment without colliding with obstacles. In practice, this removes much of the staircase-like structure produced by the raw A* path and produces a cleaner geometric path before any smoothing is attempted.

7.3.2 Path Smoothing and Arc-Length Parameterization

Following string pulling, the path consists of sparse, unevenly spaced waypoints. To produce a reference trajectory suitable for the LQR controller, we apply a **Centripetal Catmull-Rom spline** followed by a uniform resampling stage.

Spline Selection The centripetal parameterization ($\alpha = 0.5$) was chosen over the standard uniform version because it prevents the "overshoot" and unrealistic loops often seen in uniform splines when waypoints are clustered. Furthermore, as an interpolating spline, it ensures the robot passes exactly through the meaningful points defined by the pruned path.

The Parameterization Problem Standard spline evaluation uses a relative parameter $t \in [0, 1]$ for each segment. However, t does not map linearly to physical distance. Sampling at fixed increments of Δt causes the trajectory to become unevenly parameterized: long segments are sampled sparsely, while short segments are sampled densely. This creates a fluctuating geometric error signal for the LQR controller, leading to inconsistent velocity targets and visibly uneven tracking.

Uniform Resampling Implementation To ensure a consistent reference signal, the spline is re-parameterized by arc length s through a three-stage numerical process:

1. **Dense Modeling:** Each spline segment is evaluated at high resolution (100 samples per segment) to create a dense polyline approximation of the curve, denoted as points $\mathbf{q}_0, \mathbf{q}_1, \ldots, \mathbf{q}_N$.
2. **Cumulative Distance:** The discrete cumulative arc length ℓ is computed for every dense point:
$$\ell_0 = 0, \qquad \ell_k = \ell_{k-1} + \|\mathbf{q}_k - \mathbf{q}_{k-1}\|$$
3. **Linear Resampling:** The final trajectory points $\hat{\mathbf{p}}_m$ are generated at uniform spatial intervals of $\Delta s = 0.05\,\text{m}$. For a target distance $s_m = m \cdot \Delta s$, we locate the interval $\ell_k \leq s_m \leq \ell_{k+1}$ and interpolate:
$$\hat{\mathbf{p}}_m = (1 - \lambda_m)\mathbf{q}_k + \lambda_m \mathbf{q}_{k+1}, \quad \text{where} \quad \lambda_m = \frac{s_m - \ell_k}{\ell_{k+1} - \ell_k}$$

This ensures that the controller receives waypoints at a constant spatial frequency, allowing for stable velocity along the path and consistent tracking performance.

8 Trajectory Following

8.1 Linear Quadratic Regulator (LQR)

Trajectory following is performed using a Linear Quadratic Regulator (LQR). Since Paesano is a holonomic Mecanum robot operating at relatively low speed with discrete control inputs and

timings, a discrete-time kinematic model is appropriate for the controller design. Let the robot pose be

$$\mathbf{x}_k = \begin{bmatrix} x_k \\ y_k \\ \theta_k \end{bmatrix}$$

and let the control input be the commanded body velocities

$$\mathbf{u}_k = \begin{bmatrix} v_x \\ v_y \\ \omega \end{bmatrix}.$$

The pose kinematics are

$$x_k = x_{k-1} + v_x \Delta t, \qquad y_k = y_{k-1} + v_y \Delta t, \qquad \theta_k = \theta_{k-1} + \omega \Delta t.$$

This can be expressed in the standard linear state-space form as

$$\mathbf{x}_k = \mathbf{A}\mathbf{x}_{k-1} + \mathbf{B}\mathbf{u}_{k-1}$$

with

$$\mathbf{A} = \begin{bmatrix} 1 & 0 & 0 \\ 0 & 1 & 0 \\ 0 & 0 & 1 \end{bmatrix} = \mathbf{I}, \qquad \mathbf{B} = \Delta t \begin{bmatrix} 1 & 0 & 0 \\ 0 & 1 & 0 \\ 0 & 0 & 1 \end{bmatrix} = \Delta t\, \mathbf{I}.$$

The implemented controller does not regulate absolute pose directly. Instead, it computes the local pose error between the robot and the selected target waypoint, expressed in the robot frame:

$$\mathbf{e}_k = \begin{bmatrix} e_x \\ e_y \\ e_\theta \end{bmatrix}$$

Objective Function and Value Function The controller is designed to minimize the infinite-horizon quadratic cost J, which serves as the cumulative penalty for tracking error and control effort over an infinite timeline:

$$J = \sum_{k=0}^{\infty} \left(\mathbf{e}_k^T \mathbf{Q} \mathbf{e}_k + \mathbf{u}_k^T \mathbf{R} \mathbf{u}_k \right)$$

While J defines the optimization goal, the actual minimum achievable cost from a given error state is described by the **Value Function**, $V(\mathbf{e}_k) = J_{\min}$. For LQR, this value represents the total "cost-to-go" assuming an optimal policy is followed from the current time k onward. We rewrite $J_{\min}$ as a function of the tracking error:

$$J_{\min} = \mathbf{e}_k^T \mathbf{P}\, \mathbf{e}_k$$

Solving the DARE The matrix $\mathbf{P}$ is the steady-state solution to the **Discrete Algebraic Riccati Equation (DARE)**:

$$\mathbf{P} = \mathbf{A}^T \mathbf{P} \mathbf{A} - \mathbf{A}^T \mathbf{P} \mathbf{B} \left(\mathbf{R} + \mathbf{B}^T \mathbf{P} \mathbf{B} \right)^{-1} \mathbf{B}^T \mathbf{P} \mathbf{A} + \mathbf{Q}$$

In this framework, $\mathbf{P}$ acts as a compressed representation of the system's future behavior. It encodes the dynamics $(\mathbf{A}, \mathbf{B})$ and the weights $(\mathbf{Q}, \mathbf{R})$ into a constant operator that maps any current pose error into a scalar value representing the total future penalty. In the implementation, a fixed-point Riccati iteration is run at startup until $\|\mathbf{P}_{k+1} - \mathbf{P}_k\| < 10^{-6}$ or 1000 iterations have elapsed, and the resulting $\mathbf{P}$ matrix is cached for runtime use.

Control Synthesis Once $\mathbf{P}$ is determined, the optimal feedback gain $\mathbf{K}$ is

$$\mathbf{K} = \left(\mathbf{R} + \mathbf{B}^T\mathbf{P}\mathbf{B}\right)^{-1}\mathbf{B}^T\mathbf{P}\mathbf{A}$$

Since the state is defined as target-minus-current error, the feedback command used in the implementation is

$$\mathbf{u}_{fb} = \mathbf{K}\mathbf{e}$$

The total command adds a feedforward term derived from the current path segment:

$$\mathbf{u}_{total} = \mathbf{K}\mathbf{e} + \mathbf{u}_{ff}$$

In the implementation, the controller selects a target waypoint and the following waypoint and computes the segment direction

$$\Delta\mathbf{p} = \begin{bmatrix} x_{j+1} - x_j \\ y_{j+1} - y_j \end{bmatrix},$$

When this segment is nonzero and the robot is not yet capturing the final pose, a nominal translational feedforward speed of $0.35\,\mathrm{m/s}$ is assigned along the normalized segment direction. That direction is rotated into the robot frame to form the translational part of $\mathbf{u}_{ff}$. The yaw component is a proportional heading-alignment term:

$$\omega_{ff} = 0.5\,\mathrm{wrap}(\mathrm{atan2}(\Delta y, \Delta x) - \theta)\,.$$

The feedback term corrects tracking error, while the feedforward term provides nominal motion along the path.

9 Mobile Application

Paesano is operated through a custom iOS application that serves as the primary user interface for robot interaction. Rather than relying on terminal commands during normal use, the app exposes the robot's current state, map data, and navigation controls in a single interface designed for real-time operation.

The application was written in SwiftUI and connects directly to the robot over the local network using a manually entered IP address or hostname. Once connected, it uses HTTP endpoints for discrete actions such as mode switching, goal submission, map saving, and navigation pause or cancel requests. A WebSocket connection is used in parallel to stream state updates and map revisions back to the phone so the interface can update continuously without requiring constant manual refresh. On the robot side, these interfaces are exposed through a FastAPI and Uvicorn bridge that also runs as a ROS 2 node. That bridge owns mode switching by stopping the current bringup process and relaunching the robot stack in mapping or localization mode, while also translating network requests into ROS 2 actions, services, and topic publications.

The mobile interface is organized around the robot's high-level operating modes:

- **Mapping mode:** Provides joystick-based teleoperation for manual exploration while showing the occupancy map live. The user can save the resulting map directly from the application once sufficient coverage has been achieved.
- **Navigation mode:** Displays the current occupancy map, estimated robot pose, and planned path. The user can tap directly on the map to submit a navigation goal, then pause, resume, or cancel the path while observing the live telemetry response.

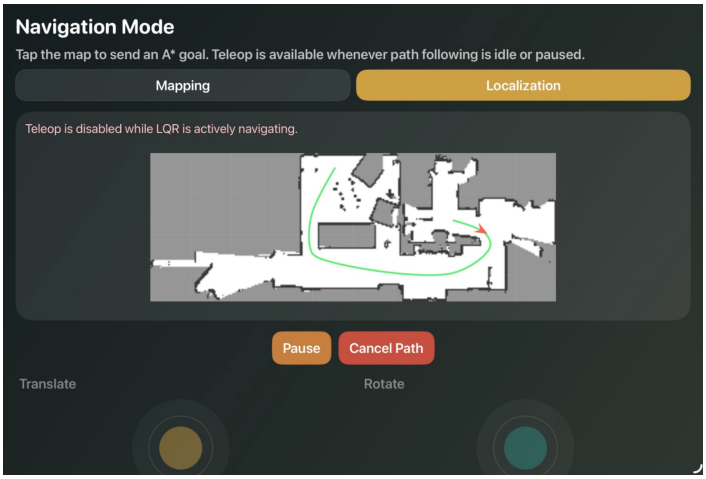

Figure 8: Paesano mobile application interface for telemetry, teleoperation, and navigation control. The screenshot shows the navigation mode.

10 Experiments

To evaluate Paesano at both the low-level control and high-level autonomy levels, two experiments were conducted. The first isolates drivetrain command tracking and stop behavior. The second evaluates the full autonomy stack by measuring how closely the robot follows planned trajectories in the map frame. Together, these experiments validate the platform from motor control through navigation execution.

10.1 Velocity and Position Control Performance

For the low-level velocity and position control tests, ROS 2 bags were recorded while forward, lateral, and rotational commands were applied over multiple different magnitudes. The bags included `/cmd_vel`, `/odom`, `/odom/filtered`, and `/wheel_encoders`. From these logs, rise behavior, overshoot, settling, and residual stop error were observed.

Table 3: Average low-level control metrics across the recorded velocity-control trials.

Motion	Mean steady-state error	Mean overshoot	Mean stop decay	Mean encoder stop error
Forward	$-0.0067\,\mathrm{m/s}$	$5.79\,\%$	$0.35\,\mathrm{s}$	$0.0097\,\mathrm{m}$
Lateral	$-0.0056\,\mathrm{m/s}$	$5.66\,\%$	$0.25\,\mathrm{s}$	$0.0073\,\mathrm{m}$
Rotation	$-0.0245\,\mathrm{rad/s}$	$11.06\,\%$	$0.33\,\mathrm{s}$	N/A

Across all three motion axes, the steady-state errors are negative, indicating that the robot consistently overtracked the commanded velocity slightly before settling. This pattern is consistent across axes and suggests a slightly aggressive feedforward bias rather than PID tuning issues. However, the magnitude of these errors is relatively small, validating the velocity PID controller's performance.

Forward and lateral tracking exhibited similar overshoot, steady-state error, and stop behavior. The encoder stop errors were also small, validating the position PID controller's performance.

Rotational tracking exhibited the largest overshoot, which is expected. Mecanum rotation requires all four wheels to coordinate through more slip-sensitive wheel-ground interactions than pure translation, making the yaw response harder to control cleanly.

The post-stop rotational decay remained short and consistent for all three axes, which is critical behavior for the higher-level navigation stack.

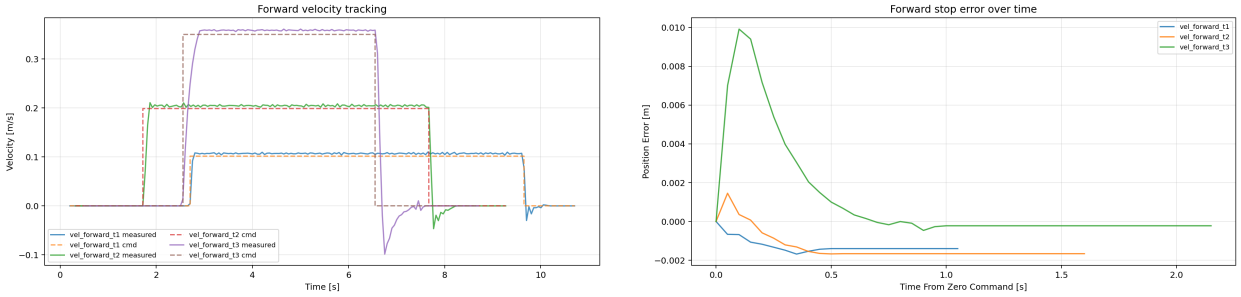

(a) Forward velocity tracking.

(b) Forward stop error after zero command.

Figure 9: Forward-axis low-level control performance. The measured response closely tracks the commanded input, with only a brief braking transient when the command returns to zero.

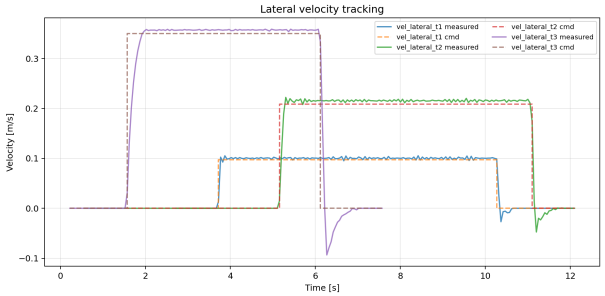

(a) Lateral velocity tracking.

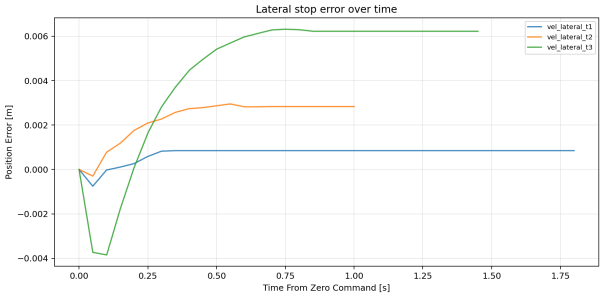

(b) Lateral stop error after zero command.

Figure 10: Lateral-axis low-level control performance. Strafing remained stable and repeatable, similar to the forward axis.

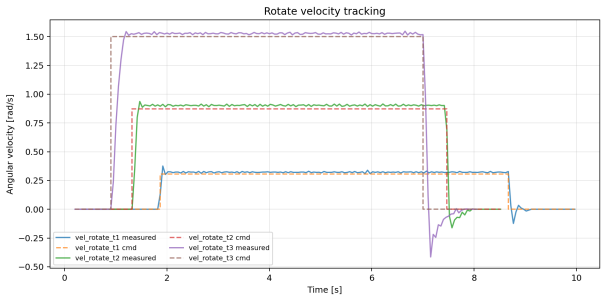

(a) Angular velocity tracking.

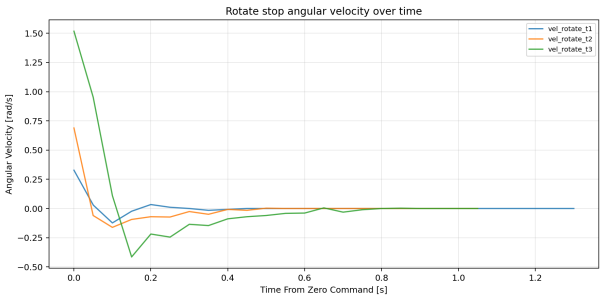

(b) Angular velocity decay after zero command.

Figure 11: Rotational low-level control performance. The turn response exhibits slightly higher overshoot than the translational axes, but the stop behavior remains sharp and repeatable.

10.2 Trajectory Following Performance

The second experiment evaluated the full autonomy stack in localization mode. Three routes were tested: a straight route, a single-turn curve route, and a longer multi-segment route through a more complex portion of the map. Each route was executed three times from a fixed marked start pose, and ROS 2 bags were recorded containing `/path`, `/estimated_pose`, `/odom/filtered`, `/cmd_vel`, and `/map`. The primary metrics were completion time, final position error, final heading error, and cross-track error with respect to the planned path.

This experiment intentionally validates more than just the tracking controller. Because the robot is operating in the map frame while using the full navigation stack, the results reflect the combined behavior of localization, global planning, path pruning, spline generation, and LQR tracking. Route-following accuracy therefore also captures localization quality implicitly, since the pose estimator must remain consistent over the full run for the robot to remain on the planned path.

Table 4: Average trajectory-following results by route type.

Route	Mean completion time	Mean final position error	Mean cross-track error	Mean final heading error	Success
Straight	6.11 s	0.0041 m	0.0089 m	0.154 deg	3/3
Curve	18.29 s	0.0041 m	0.0086 m	0.366 deg	3/3
Complex	44.09 s	0.0095 m	0.0087 m	0.270 deg	3/3

Across all nine recorded navigation runs, the mean cross-track error in the LiDAR-localized map frame was 0.0088 m, the mean final position error was 0.0059 m, the mean final heading error was 0.263 deg, and every trial completed successfully. These values validate the overall performance of Paesano and indicate that the path planner, spline generator, and LQR tracker are all operating consistently in the same frame as the localization estimate. Because the metric is computed from the estimated pose and planned path in the map frame rather than from an external ground-truth system, it should be interpreted as estimated route-following accuracy relative to the localization estimate rather than absolute physical accuracy.

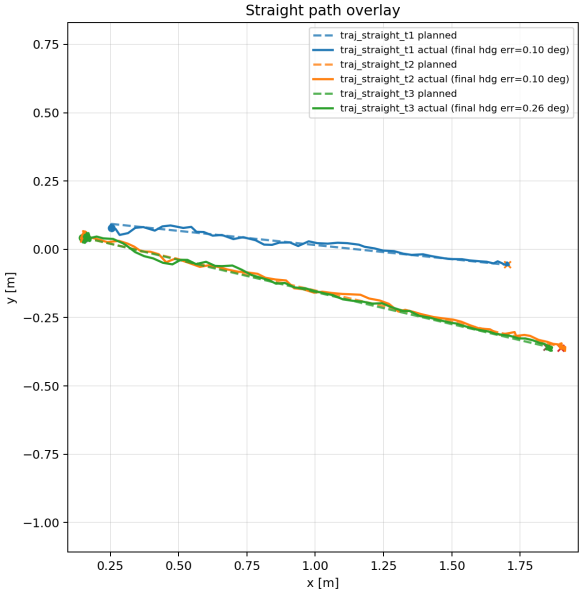

(a) Straight-route planned and actual paths.

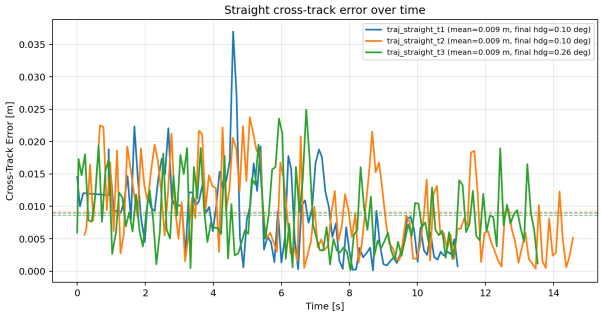

(b) Straight-route cross-track error over time.

Figure 12: Trajectory-following results for the straight route. The actual path remains nearly coincident with the planned reference, and the cross-track error stays small throughout the run.

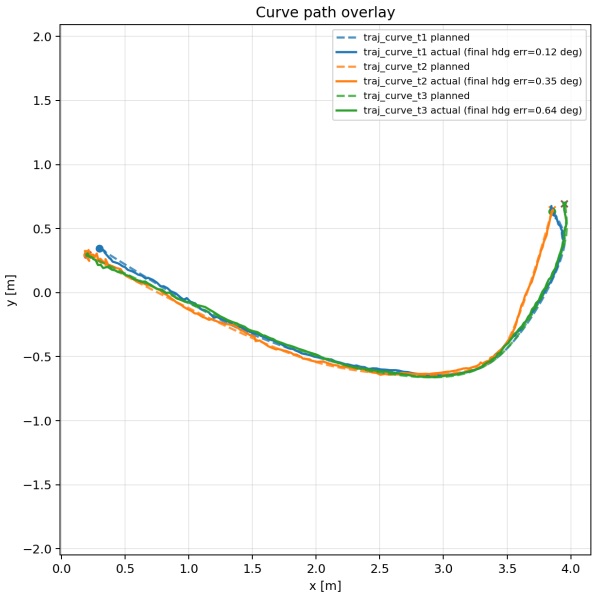

(a) Curve-route planned and actual paths.

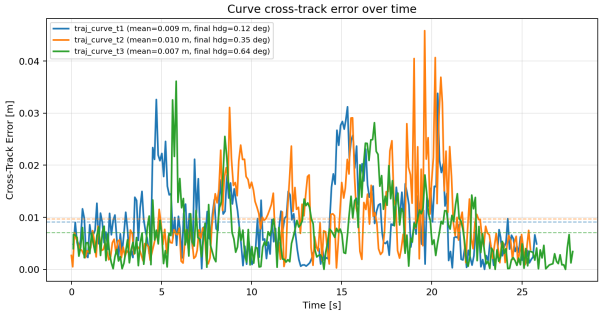

(b) Curve-route cross-track error over time.

Figure 13: Trajectory-following results for the single-turn curve route. The controller remains tightly aligned with the planned reference through the turn.

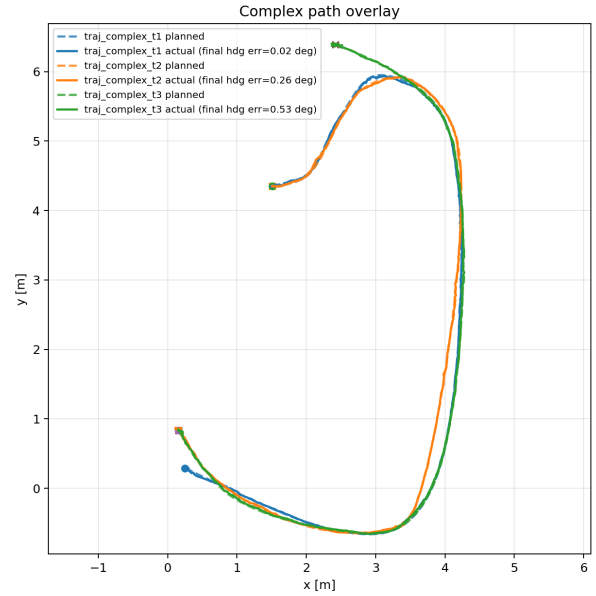

(a) Complex-route planned and actual paths.

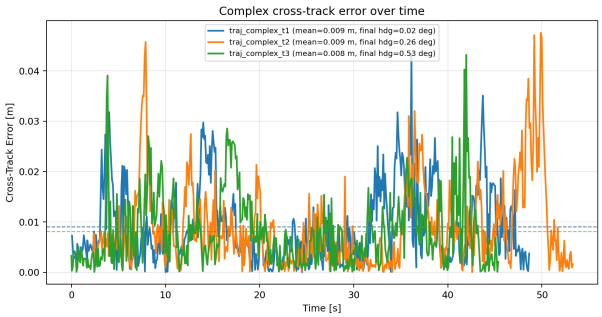

(b) Complex-route cross-track error over time.

Figure 14: Trajectory-following results for the complex multi-segment route. Even on the longest path, the measured tracking error remains small relative to the map scale.

11 Conclusion and Future Improvements

11.1 Conclusion

I started this project the second month of my first semester. I assumed it would be a few months-long process that could be completed by the end of the semester, but it ended up my entire first year and I still plan on continuing. The layers of complexity were invisible to me at the time, and in all honesty, I am glad that I didn't know how much work it would be when I started, because it was a nice surprise to learn about things that I didn't even know existed!

11.2 Problems Encountered

There were many problems that arose along the way. The first was part selection. Finding the best sensors at the lowest cost and making sure everything was compatible was a major challenge. The second was the power architecture. Going into this project, I had little experience designing power systems, even at this scale. I had to learn about different types of batteries, voltage regulation, power distribution, and how to ensure each system got the necessary voltage and current without overloading or underpowering anything.

The next was the firmware and low-level control module itself. Since the HiWonder chassis was a black box of sorts, finding out which motor wire corresponded to which direction and which ones were the encoders was a difficult process, and then knowing which side of the encoder signal was A and which was B was another challenge. It required a lot of tuning and trial and error. Because I designed the motor control module so that the encoder pins and motor pins are jumper wires that can be connected in any which way, I was able to test different configurations until I found the one that worked, but it was a time-consuming process. Low level motor control is a very different problem than high-level autonomy, and I had to learn how to write a reliable embedded control loop that could use a velocity PID controller for velocity tracking and a position PID controller to stop at the right location.

In terms of the ROS 2 stack, the first major challenge was the localization stack. Implementing the particle filter and tuning its parameters to work well with the EKF and my specific sensor setup was extremely difficult. Maintaining a consistent TF tree: validating that the particles, robot, and pose estimate were all in the correct frame and that there were not multiple competing TF publishers was a major source of bugs and confusion. After this hurdle was crossed, tuning the parameters of the particle filter to be stable under normal navigation but also to recover from localization degradation took significant trial and error.

Path planning and trajectory generation was the next big challenge I faced. Implementing the A* search on the grid itself was straightforward, but modelling the environment with an inflated cost map to produce wider clearance paths wasn't necessarily intuitive at first. Then the post-processing pipeline to convert the jagged A* output into a smooth, approximately arc-length-resampled trajectory suitable for LQR tracking took a lot of research and tuning to get right. I tried many different algorithms, such as B-splines, uniform Catmull-Rom splines, and cubic Hermite splines, before settling on the centripetal Catmull-Rom version, which I determined to be the most suitable for the application. While LQR itself was a straightforward choice for the controller, tuning the $\mathbf{Q}$ and $\mathbf{R}$ matrices to achieve good tracking performance without excessive control effort took a lot of experimentation. However, after it was all said and done, Paesano is able to perform extremely

consistently, and the amount that I have learned from the full stack development of this robot has been invaluable.

11.3 Future Improvements

There are several directions I want to take Paesano next. The most immediate is dynamic obstacle avoidance. The current planner has no awareness of moving objects, which means a person walking into the path will either cause a collision or force a full replan. A local avoidance layer that reacts to real-time LiDAR data while still following the global path would make the system actually usable in a lived-in environment.

I want to move beyond purely geometric control and give the robot some awareness of its surroundings. Right now it treats a doorway the same as any other free cell. Higher-level semantic reasoning could enable behaviors like slowing near doorways, avoiding crowded areas, or following a person: the kinds of things that would make Paesano useful rather than just functional.

Finally, the experiments in this report measure accuracy relative to the internal map frame rather than external ground truth. I would like to set up a proper ground truth evaluation using a motion capture system or visual odometry to get an honest measurement of absolute localization accuracy, since the current metrics only capture how internally consistent the stack is, not how close the robot actually is to where it thinks it is.